# Supporting Information

Sun et al. 10.1073/pnas.1217203110

## SI Results and Discussion

**Yeast and Human CRM1 Bind Leptomycin B Similarly.** The regions of human and *Saccharomyces cerevisiae* chromosomal region maintenance 1 (CRM1) proteins that form the nuclear export signal (NES) -binding grooves (residues 510–595 in $^{Hs}$CRM1 and residues 521–605 in $^{Sc}$CRM1) share 81% sequence identity (Fig. 1*D*). Almost all CRM1 residues involved in NES and inhibitor binding are strictly conserved. Nevertheless, the small difference in sequence of residues that line the $^{Hs}$CRM1 and $^{Sc}$CRM1 grooves near the LMB active site prompted us to mutate segment $^{537}$DLTVK$^{541}$ of $^{Sc}$CRM1 to GLCEQ to mimic the $^{Hs}$CRM1 sequence. Structure of the Leptomycin B (LMB) -bound grooves of $^{Sc}$CRM1($^{537}$DLTVK$^{541}$/GLCEQ) and $^{Sc}$CRM1* are virtually identical (Cα rmsd of 0.24 for CRM1 residues; all-atom rmsd of 0.14 for LMB), suggesting that the yeast and human CRM1 grooves bind LMB similarly (Figs. S1 *A* and *B* and S2 *A* and *B* and Table S2).

We have explained the mechanism of LMB hydrolysis by $^{Sc}$CRM1*. We can strongly infer that this mechanism of inhibition also occurs in $^{Hs}$CRM1, although the human protein has not crystallized with LMB. First, LMB-bound grooves of $^{Sc}$CRM1* and $^{Sc}$CRM1($^{537}$DLTVK$^{541}$/GLCEQ), which mimics the $^{Hs}$CRM1 sequence, are virtually identical (see above), suggesting that the yeast and human CRM1 grooves bind LMB similarly. Second, $^{Hs}$CRM1 and $^{Sc}$CRM1* exhibit similar inhibition trends for LMB vs. chemically hydrolyzed LMB (Fig. 4*C*), and third, CRM1-mediated nuclear export in the CRM1T539C *S. cerevisiae* strain, where Thr-539 of $^{Sc}$CRM1 is mutated to cysteine, is similarly sensitive to LMB as mammalian cells (1). MS results of $^{Sc}$CRM1* and LMB-$^{Sc}$CRM1* provide support for hydrolyzed LMB conjugated to CRM1 that is independent of our crystallographic findings (Fig. 4*A*). $^{13}$C-NMR analysis of CRM1-bound LMB is hindered by the current unavailability of $^{13}$C-LMB and the LMB-producing streptomyces strain (2) in the public domain.

**Comparison of Computational Model and Crystal Structure of the CRM1-LMB Complex.** LMB and CRM1 are both flexible molecules, although previous work suggested otherwise. The LMB-bound groove is narrower and deeper than the NES-bound groove as a result of helix and sidechain reorientations. Therefore, it is not surprising that computational modeling of LMB into the wider and shallower NES-bound groove produced a model that is quite different from our crystal structures (3). LMB molecules in the model and our structures bind the CRM1 groove in grossly similar directions. However, beyond this trivial similarity, their modes of interaction with CRM1 differ significantly. These differences are largely because of conformational changes of the CRM1 groove and also hydrolysis of the LMB lactone by CRM1, which were revealed entirely and unexpectedly by our structures.

Differences between a previously reported computational model (3) and our crystal structure are as follows. (*i*) LMB bound as a lactone in the computational model, whereas the crystal structure showed that the lactone ring of LMB was hydrolyzed (Fig. 3*A*). Lactone hydrolysis could not have been predicted by computational modeling. (*ii*) LMB in the computational model is conjugated to CRM1 in the S configuration. In the X-ray structures, LMB (both lactone and hydroxy acid forms) bound in the R configuration, which is accommodated by numerous interactions in a conformationally rearranged groove (Fig. 3*A*). (*iii*) The polyketide portion of LMB is quite flexible because of many rotatable C-C bonds, thus making modeling difficult and unreliable (3). This problem is further compounded by CRM1 groove plasticity (Fig. 2). As a result, the modeled LMB is mostly straight (3), whereas LMBs in our crystal structures make two ∼90° turns to penetrate deep into the groove (Figs. 2*C* and 3*A*). (*iv*) The different orientations and chemical structures of LMB in the computational and X-ray models placed chemical groups in different vertical positions along the grooves. In the computational model, the hydrophobic position Φ1 of NES overlaps with LMB C31, NES Φ2 overlaps with LMB C29, and NES Φ3 overlaps with LMB C27 (3). The X-ray structures are very different, with NES Φ1 overlapping with LMB C32, NES Φ2 overlapping with LMB C28, and NES Φ3 overlapping with C4 and C5 of the hydroxy acid of LMB (Fig. 2*C*).

## SI Materials and Methods

**Cloning, Expression, and Protein Purification.** $^{Hs}$Ran was cloned into the pET18 vector. $^{Sc}$CRM1 and $^{Sc}$RanBP1 were cloned into a pGEX-4t-3–based expression vector with a tobacco etch virus protease-cleavable N-terminal GST tag. Residues 377–413 of $^{Sc}$CRM1 were removed as previously described (4), and Thr-539 was mutated to cysteine to generate the inhibitor-accessible $^{Sc}$CRM1* protein. Ten different $^{Sc}$CRM1 mutants (Tables S2–S4) were generated by site-directed mutagenesis using PCR. $^{Sc}$CRM1, $^{Sc}$RanBP1, and $^{Hs}$Ran were expressed separately in *Escherichia coli* BL-21 (DE3) after induction with 0.5 mM isopropyl β-D-1-thiogalactopyranoside for 10 h at 25 °C. The three proteins were purified separately. GST-$^{Sc}$CRM1 and GST-$^{Sc}$RanBP1 were purified by glutathione Sepharose (GE Healthcare) affinity chromatography, cleaved off the beads with TEV protease, and further purified by gel filtration chromatography in buffer containing 10 mM Tris, pH 7.5, 100 mM NaCl, and 5 mM $MgCl_2$. His-tagged $^{Hs}$Ran was purified by affinity chromatography using Ni-NTA beads (QIAGEN), eluted with buffer containing 20 mM Tris, pH 7.5, 10% glycerol, 200 mM Imidazole, and 200 mM NaCl, and further purified by gel filtration in buffer containing 10 mM Tris, pH 7.5, 100 mM NaCl, and 5 mM $MgCl_2$. $^{Hs}$Ran was loaded with nucleotide analog 5′-Guanylyl imidodiphosphate (GppNHp) as previously described (5). $^{Sc}$CRM1*-$^{Hs}$Ran-$^{Sc}$RanBP1 complexes were obtained by mixing the three proteins at a 1:2:1.5 molar ratio followed by gel filtration chromatography. The purified protein complexes were then mixed with CRM1 inhibitors (Enzo Life Sciences) at a 1:2 molar ratio. The $^{Sc}$CRM1(T539S)-$^{Hs}$Ran-$^{Sc}$RanBP1 complex was mixed with LMB at a 1:10 molar ratio to achieve maximum noncovalent binding of the inhibitor.

**Crystallization, Data Collection, Structure Determination, and Refinement.** Crystals of the CRM1 inhibitor complexes grew in 1–2 d in conditions similar to those conditions used by Koyama and Matsuura (4) (reservoir solution 18% PEG3350, 200 mM ammonium nitrate, 100 mM Bis·Tris, pH 6.6). Crystallization solutions were supplemented with 20% (vol/vol) glycerol to cryoprotect the crystals. X-ray diffraction data were collected at beamline 19ID, Advanced Photon Source, Argonne National Laboratory (Tables S1–S4). The structures were solved using the molecular replacement program MolRep (6) and the coordinates of $^{Sc}$CRM1-$^{Sc}$Ran-$^{Sc}$RanBP1 (Protein Data Bank ID code 3M1I) (4) as the search model. One inhibitor-$^{Sc}$CRM1*-$^{Hs}$Ran-$^{Sc}$RanBP1 complex is present in each asymmetric unit. The resulting models and electron density maps were examined with the program COOT (7). Several cycles of model rebuilding and refinement using the program Refmac5 (8) led to convergence. Translation/

Libration/Screw refinement was used in the refinement process (9). Ramanchandran statistics were calculated using the CCP4 program Procheck (10).

**Chemical Analysis of LMB Hydrolysis Products by NMR and LC-MS.** $^{1}$H-NMR spectra of LMB at pH values of 3.0, 5.0, 7.0, 8.5, and 10 were measured in 30% $CD_3OD/D_2O$ at 600 MHz. LMB was dissolved in $D_2O$ buffer that mimics the crystallization buffer (10 mM Bis·Tris, pH 6.6, 100 mM ammonium nitrate, 5% PEG, 1 mM Tris, pH 7.5, 50 mM sodium chloride, 2.5 mM magnesium acetate). Data were acquired 10 min after pH adjustment. LC-MS analysis of LMB + DTT in buffer and LMB in buffer (no DTT) were analyzed by LC-UV-MS using a Phenomenex C18 Luna HPLC column (4.6 × 100 mm) with a solvent gradient from 90:10 $H_2O$:$CH_3CN$ to 0:100 $H_2O$:$CH_3CN$ over 17 min and then, 0:100 $H_2O$:$CH_3CN$ for 10 min. Detection of LMB, LMB + DTT, and hydrolyzed LMB + DTT was accomplished at 254 nm and with MS $[M + H]^+$.

**Intact Protein Mass Determination.** The modification reaction for MS analysis was carried out by incubating $^{Sc}$CRM1* with LMB at room temperature for 10 min. The pH of the reaction solution was then lowered using 1% trifluoroacetic acid (TFA) solution to a final concentration of 0.1%, and the sample was injected immediately for trapping and MS analysis. In-line desalting was achieved using a reversed phase trap and self-packed with PO-ROS R1 20 μm 4,000-Å media (Applied Biosystems). Proteins were captured by the trap in 100% water and 0.1% formic acid and eluted in 50% acetonitrile, 50% trifluoroethanol, and 0.5% formic acid using a 5-μL/min flow rate delivered by a syringe pump. All analyses were performed using a 6540 Ultra High-Definition Accurate-Mass Q-TOF mass spectrometer equipped with a Jet Stream ESI source (Agilent Technologies). Data were acquired in 4-GHz high-resolution mode with *m/z* range of 700–3,200 and a cycle time of 1.0 s. Data were then analyzed using the Maximum Entropy deconvolution algorithm from Agilent, which generates average masses of the target proteins by transforming the *m/z* raw spectrum into a zero-charge mass spectrum in Dalton units. Two MS experiments are shown in Fig. 4*A*. There is no obvious difference in the conditions for these two experiments. We suspect that LMB hydroxy acid is unstable in MS conditions and tends to cyclize at the low pH or gas phase ionization conditions of the experiment. The larger mass for the modification in Fig. 4*A*, *Left* implies the presence of some higher-molecular weight LMB hydroxy acid. The expected molecular mass for the LMB hydroxy acid is 558 Da. The observed molecular mass increase of 555 Da may be caused by a mixed population of LMB hydroxy acid and lactone, which cannot be resolved by MS of a 120-KDa protein. Most of the LMB hydroxy acid has recyclized in the right panel.

**LC-MS/MS Analysis.** A molar ratio of 1:2 $^{Sc}$CRM1*:LMB samples was separated by SDS/PAGE and stained with Coomassie blue. The excised gel bands were chopped into 1-mm$^3$ cubes and in-gel–digested using elastase. Coomassie blue stain was removed after 30 min incubation at 37 °C in 50 mM triethylammonium bicarbonate/acetonitrile (1:1; vol/vol), and the gel pieces were dehydrated with acetonitrile at room temperature followed by reduction/alkylation using DTT and iodoacetamide. The gel pieces were then dehydrated and rehydrated again with solution containing elastase for overnight digestion at 37 °C. Peptides were extracted using 30 min incubation at 37 °C with extraction buffer (50% acetonitrile and 3.3% TFA), and salts were removed using the Oasis HLB μElution plate (Waters) before LC-MS/MS analysis. 1D LC was performed on an Ultimate 3000 nano HPLC system (Dionex) using reverse-phase ReproSil-Pur C18-AQ 1.9-μm resin column (Dr. Maisch GmbH). Separation of peptides was carried out at 400 nL/min by a 60-min linear gradient of 1–41% acetonitrile in 0.1% formic acid. Column temperature was raised and maintained at 70 °C using a butterfly heater (Phoenix S&T, Inc.). MS analyses were performed on a Q Exactive instrument (Thermo Electron) using a data-dependent top20 method, with the full MS scans acquired at 70,000 resolution (at *m/z* 200) and MS/MS scans acquired at 17,500 resolution (at *m/z* 200). Underfill ratio was set at 0.3%, with a 3 *m/z* isolation window and fixed first mass of 100 *m/z* for the MS/MS acquisitions. The charge exclusion was applied to exclude the unassigned and charge 1 species, and dynamic exclusion was used with a duration of 15 s. Peptide coverage of $^{Sc}$CRM1* was excellent at 90%, but the LMB-modified peptide was not identified. We detected only the unmodified peptide, although LMB was added in molar excess under conditions where we see complete inhibition of NES binding. We suspect that LMB conjugation is unstable after the binding site is destroyed by proteolysis, the modification does not survive MS ionization intact, and/or LMB modification drastically affects fragmentation, preventing identification.

**Chemical Hydrolysis of LMB.** LiOH (50 μL) in tetrahydrofuran (THF)/$H_2O$ (10 μg LiOH, 3.0 μL THF, 0.5 μL $H_2O$) was added to 405 μg LMB in 200 μL THF. The mixture was stirred at room temperature under an $N_2$ atmosphere for 3 h. The hydrolysate was neutralized with HCl, diluted with water, subjected to a $C_{18}$ SEP-PAK (0.5 × 1.0 cm; Waters), and eluted with water followed by methanol. The elution was analyzed by LC-MS and purified by RP-HPLC (Phenomenex Luna, Phenyl-Hexyl; 5 mm, 250 × 10.0 mm, UV = 210 nm, 2.5-mL/min flow rate) using a gradient solvent system from 60% to 99% $CH_3CN$ (0.1% formic acid) over 30 min to yield the desired product (300 μg, $t_R$ = 10.5 min). electrospray ionization (ESI)-MS: 557 $[M - H]^-$, 581 $[M + Na]^+$.

**In Vitro NES-Binding and Inhibition Assays.** To assess CRM1–NES interactions or CRM1 inhibition, either CRM1 proteins or inhibitor-CRM1 complexes were incubated with 10 μg immobilized GST-$^{MVM\text{-}NS2}$NES in a total volume of 100 μL for 30 min at 4 °C. After extensive washing with buffer containing 50 mM Tris, pH 7.5, 110 mM potassium acetate, 20% glycerol, 1 mM EGTA, 2 mM magnesium acetate, and 2 mM DTT, bound proteins were separated by SDS/PAGE and visualized by Coomassie staining. To compare the potency of LMB or chemically hydrolyzed LMB, 120 μg purified $^{Hs}$CRM1 or $^{Sc}$CRM1* were incubated with 20 μM of either LMB or chemically hydrolyzed LMB in total volumes of 100 μL for 10 min at 4 °C and then added to immobilized GST-$^{MVM\text{-}NS2}$NES for the binding assays above. To assess the reversibility of inhibitor conjugation, 2 nmol either $^{Sc}$CRM1* or $^{Sc}$CRM1* (K541Q,K542Q,R543S,K545Q,K548Q,K579Q) were mixed with 4 nmol LMB or 10 nmol KPT185 in total volumes of 200 μL. Triplicate samples were (*i*) used as controls of fully inhibited CRM1 and subjected immediately to CRM1 inhibition assays (above), (*ii*) dialyzed against buffer containing 10 mM Tris, pH 7.5, 100 mM NaCl, 5 mM $MgCl_2$, and 2 mM DTT for 24 h at 25 °C, or (*iii*) treated with 20 mM DTT at 25 °C for 24 h. CRM1 inhibition assays were then performed using immobilized GST-$^{MVM\text{-}NS2}$NES and $^{Hs}$Ran as described above. To compare the intensities of the different CRM1 bands of SDS/PAGE gels and estimate the extent of CRM1 deconjugation, we scanned the dried gels with a desktop scanner (Epson V300) and processed images with the ImageJ software (intensity inverted, background subtracted). The intensity of each band plus three background sites were measured by drawing a fixed shape closely surrounding the band and integrating the densities. Band intensities were corrected for background and the slightly different amounts of GST-NES in each lane. GST-NES band intensities of lanes 1–5 were normalized to the band

intensity of lane 1, GST-NES band intensities of lanes 6–8 were normalized to the band intensity of lane 6, and the respective CRM1 band intensities were corrected with the normalization factors. The same gels were scanned three times, and the mean corrected CRM1 band intensities and errors were plotted on histograms in Fig. S12.


1. Neville M, Rosbash M (1999) The NES-Crm1p export pathway is not a major mRNA export route in Saccharomyces cerevisiae. *EMBO J* 18(13):3746–3756.
2. Hamamoto T, Gunji S, Tsuji H, Beppu T (1983) Leptomycins A and B, new antifungal antibiotics. I. Taxonomy of the producing strain and their fermentation, purification and characterization. *J Antibiot (Tokyo)* 36(6):639–645.
3. Bonazzi S, et al. (2010) Anguinomycins and derivatives: Total syntheses, modeling, and biological evaluation of the inhibition of nucleocytoplasmic transport. *J Am Chem Soc* 132(4):1432–1442.
4. Koyama M, Matsuura Y (2010) An allosteric mechanism to displace nuclear export cargo from CRM1 and RanGTP by RanBP1. *EMBO J* 29(12):2002–2013.
5. Chook YM, Blobel G (1999) Structure of the nuclear transport complex karyopherin-beta2-Ran x GppNHp. *Nature* 399(6733):230–237.
6. Vagin A, Teplyakov A (1997) MOLREP: An automated program for molecular replacement. *J Appl Crystallogr* 30(6):1022–1025.
7. Emsley P, Cowtan K (2004) Coot: Model-building tools for molecular graphics. *Acta Crystallogr D Biol Crystallogr* 60(Pt 12 Pt 1):2126–2132.
8. Murshudov GN, Vagin AA, Dodson EJ (1997) Refinement of macromolecular structures by the maximum-likelihood method. *Acta Crystallogr D Biol Crystallogr* 53(Pt 3):240–255.
9. Painter J, Merritt EA (2006) Optimal description of a protein structure in terms of multiple groups undergoing TLS motion. *Acta Crystallogr D Biol Crystallogr* 62(Pt 4): 439–450.
10. Laskowski RA, MacArthur MW, Moss DS, Thornton JM (1993) PROCHECK—a program to check the stereochemical quality of protein structures. *J Appl Crystallogr* 26(Pt 2):283–291.


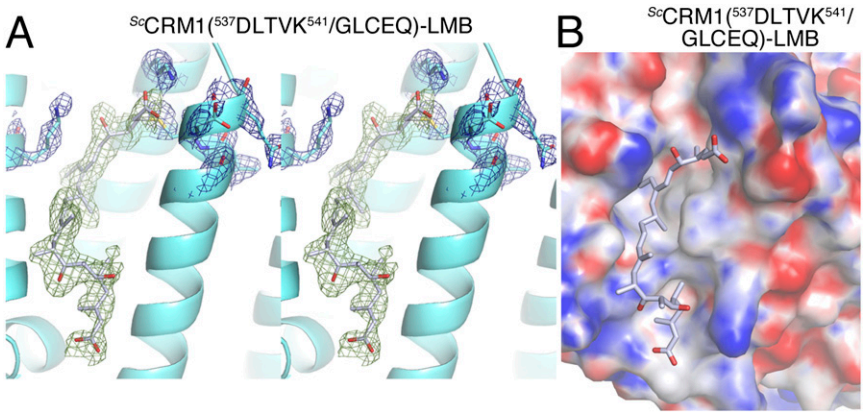


**Fig. S1.** The groove of $^{SC}$CRM1($^{537}$DLTVK$^{541}$/GLCEQ) bound to LMB. (*A*) Omit map electron densities for LMB (green) and interacting $^{SC}$CRM1($^{537}$DLTVK$^{541}$/GLCEQ) residues (blue) are displayed at 1σ cutoff. (*B*) Electrostatic surface potential (scaled at ±15 kT) of CRM1 in $^{SC}$CRM1($^{537}$DLTVK$^{541}$/GLCEQ)-LMB. The inhibitor is omitted during charge calculation.

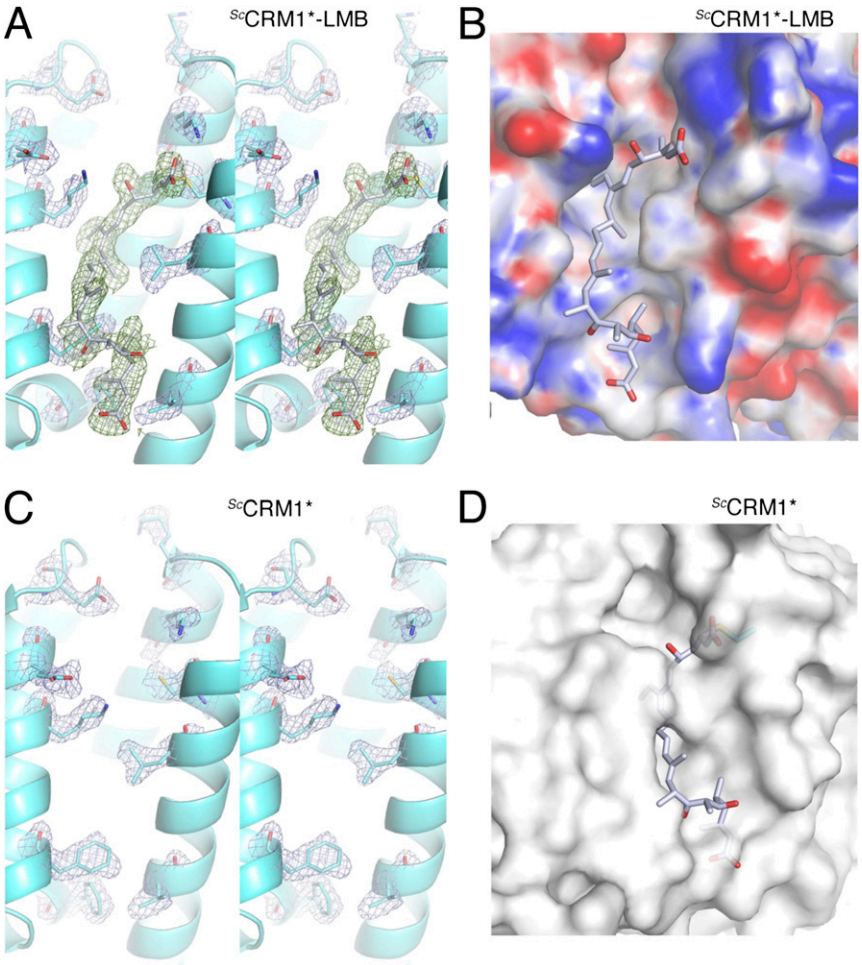


**Fig. S2.** NES-binding grooves of $^{SC}$CRM1*-LMB and $^{SC}$CRM1*. (*A*) Omit map electron densities for LMB (green) and interacting CRM1 residues (blue) are displayed at 1σ cutoff. (*B*) Electrostatic surface potential (scaled at ±15 kT) of CRM1 in $^{SC}$CRM1*-LMB. LMB is omitted during charge calculation. (*C*) Omit map electron density for selected residues (blue) in the unliganded $^{SC}$CRM1* groove displayed with 1σ cutoff. (*D*) Surface representation of the unliganded $^{SC}$CRM1* groove. LMB from $^{SC}$CRM1*-LMB structure is superimposed as reference.

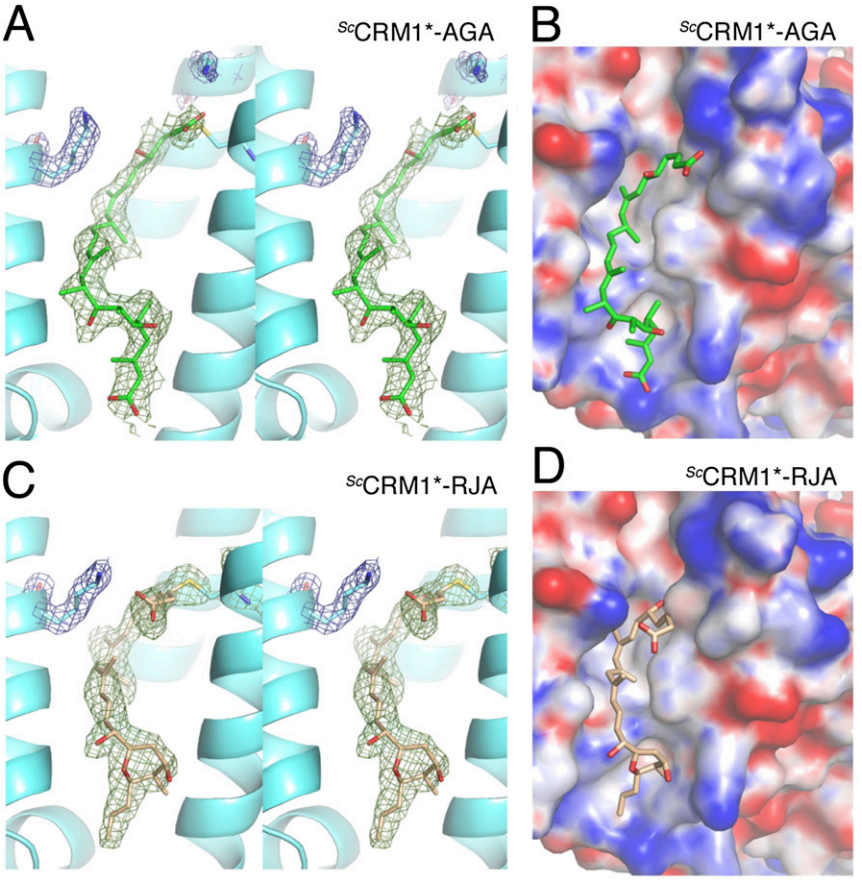


**Fig. S3.** NES-binding grooves of $^{Sc}$CRM1*-Anguinomycin A (AGA) and $^{SC}$CRM1*-Ratjadone A (RJA). (*A*) Omit map electron densities for AGA (green) and interacting CRM1 residues (blue) are displayed at 1σ cutoff. (*B*) Electrostatic surface potential (scaled at ±15 kT) of CRM1 in $^{SC}$CRM1*-AGA. AGA is omitted during charge calculation. (*C*) Omit map electron densities (green) for RJA and interacting CRM1 residues (blue) displayed at 1σ cutoff. (*D*) Electrostatic surface potential (scaled at ±15 kT) of CRM1 in $^{SC}$CRM1*-RJA. The inhibitor is omitted during charge calculation.

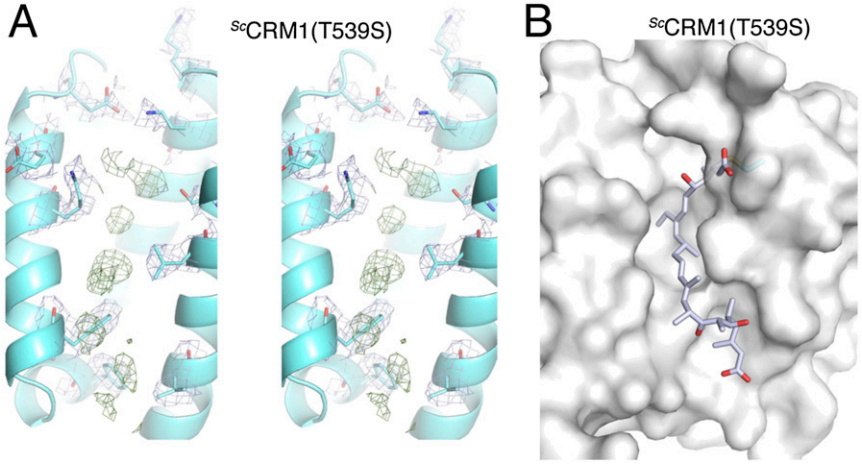


**Fig. S4.** NES-binding groove of $^{SC}$CRM1(T539S). We cocrystallized excess LMB with $^{Sc}$CRM1(T539S)-Ran-RanBP1, where a serine rather than threonine at position 539 more closely mimics the reactive cysteine. The 2.8-Å resolution structure shows that the CRM1 groove is open, but LMB is not modeled because of weak electron density in the groove. (*A*) Omit map electron densities for select $^{SC}$CRM1(T539S) residues (blue) in the groove are displayed with 1σ cutoff. Weak densities observed in groove are shown in green. (*B*) Surface representation of the $^{SC}$CRM1(T539S) groove. LMB from $^{SC}$CRM1*-LMB structure is superimposed as reference.

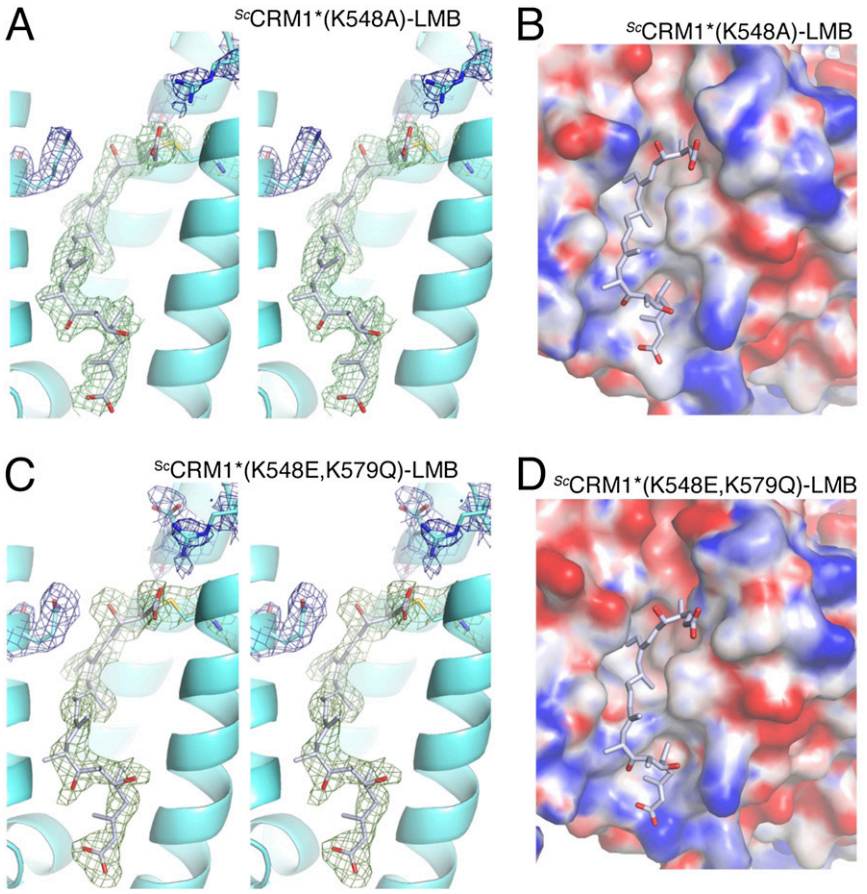


**Fig. S5.** NES-binding grooves of $^{sc}$CRM1*(K548A)-LMB and $^{SC}$CRM1*(K548E,K579Q)-LMB. (*A*) Omit map electron densities (green) for LMB and interacting $^{sc}$CRM1*(K548A) residues (blue) displayed at 1σ cutoff. (*B*) Electrostatic surface potential (scaled at ±15 kT) of CRM1 in $^{sc}$CRM1*(K548A)-LMB. The inhibitor is omitted during charge calculation. (*C*) Omit map electron densities for LMB (green) and interacting $^{SC}$CRM1*(K548E,K579Q) residues (blue) displayed at 1σ cutoff. (*D*) Electrostatic surface potential (scaled at ±15 kT) of CRM1 in $^{SC}$CRM1*(K548E,K579Q)-LMB. The inhibitor is omitted during charge calculation.

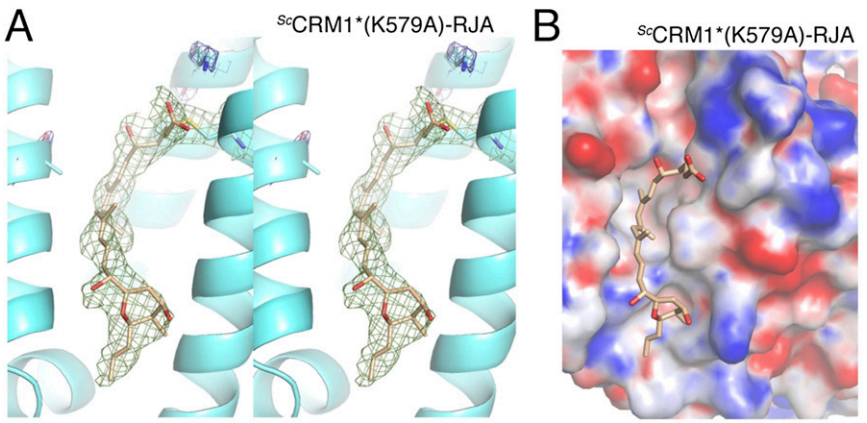


**Fig. S6.** NES-binding grooves of $^{sc}$CRM1*(K579A)-RJA. (*A*) Omit map electron densities for RJA (green) and interacting $^{sc}$CRM1*(K579A) residues (blue) displayed at 1σ cutoff. (*B*) Electrostatic surface potential (scaled at ±15 kT) of CRM1 in $^{sc}$CRM1*(K579A)-RJA. The inhibitor is omitted during charge calculation.

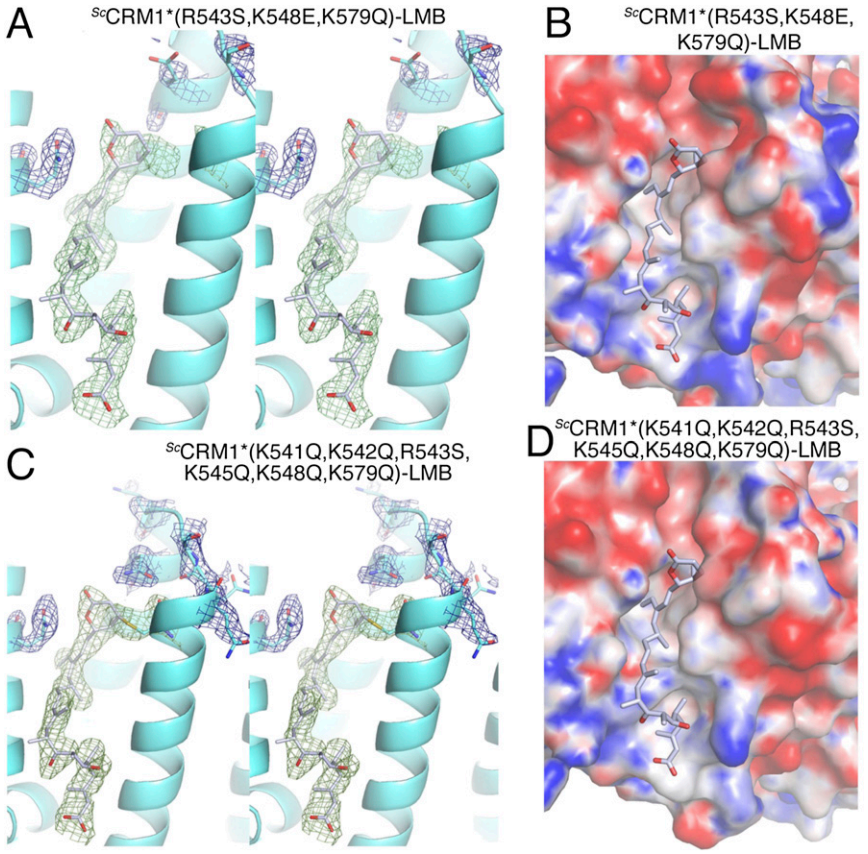


**Fig. S7.** NES-binding grooves of $^{sc}$CRM1*(R543S,K548E,K579Q)-LMB and $^{SC}$CRM1*(K541Q, K542Q,R543S,K545Q,K548Q,K579Q)-LMB. (*A*) Omit map electron densities for LMB (green) and interacting $^{sc}$CRM1*(R543S, K548E, K579Q) residues (blue) displayed at 1σ cutoff. (*B*) Electrostatic surface potential (scaled at ±15 kT) of CRM1 in $^{sc}$CRM1*(R543S,K548E,K579Q)-LMB. The inhibitor is omitted during charge calculation. (*C*) Omit map electron densities for LMB (green) and interacting $^{SC}$CRM1*(K541Q, K542Q,R543S,K545Q,K548Q,K579Q) residues (blue) displayed at 1σ cutoff. (*D*) Electrostatic surface potential (scaled at ±15 kT) of CRM1 in $^{SC}$CRM1*(K541Q, K542Q,R543S,K545Q,K548Q,K579Q)-LMB. The inhibitor is omitted during charge calculation.

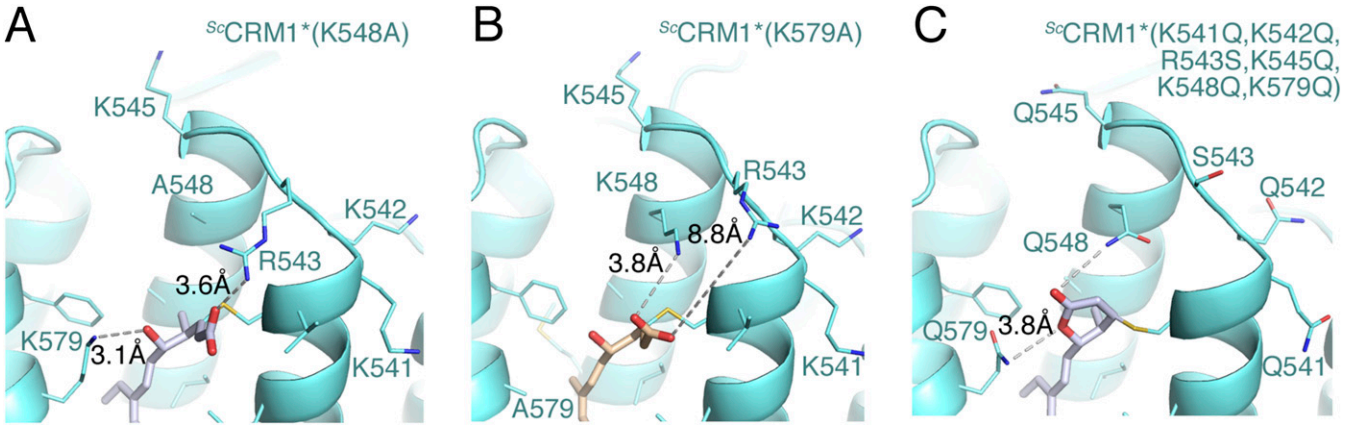


**Fig. S8.** Structures of LMB and RJA in the grooves of the $^{sc}$CRM1 mutants. (*A–C*) Reaction sites of the inhibitors (light blue, LMB; brown, RJA). $^{sc}$CRM1 mutants (aquamarine) are shown in cartoon representations, and residues that contact the inhibitors are shown as line drawings.

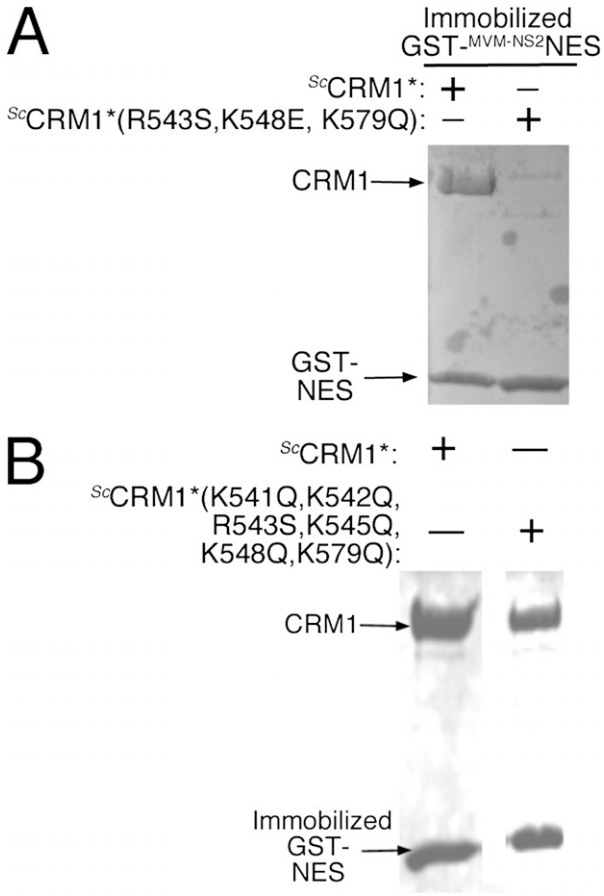


**Fig. S9.** Arg-543, Lys-548, and Lys-579 are important for NES binding. (*A*) Mutant $^{Sc}$CRM1*(R543S,K548E,K579Q) does not bind GST-$^{MVM\text{-}NS2}$NES; 10 μM $^{Sc}$CRM1* or $^{Sc}$CRM1*(R543S,K548E,K579Q) mutant is added to 5 μM immobilized GST-NES. After extensive washing, bound proteins are separated and visualized by SDS/PAGE and Coomassie staining. (*B*) Affinity of mutant $^{Sc}$CRM1*(K541Q,K542Q,R543S,K545Q,K548Q,K579Q) for GST-NES is decreased. Assay similar to the assay described for *A*.

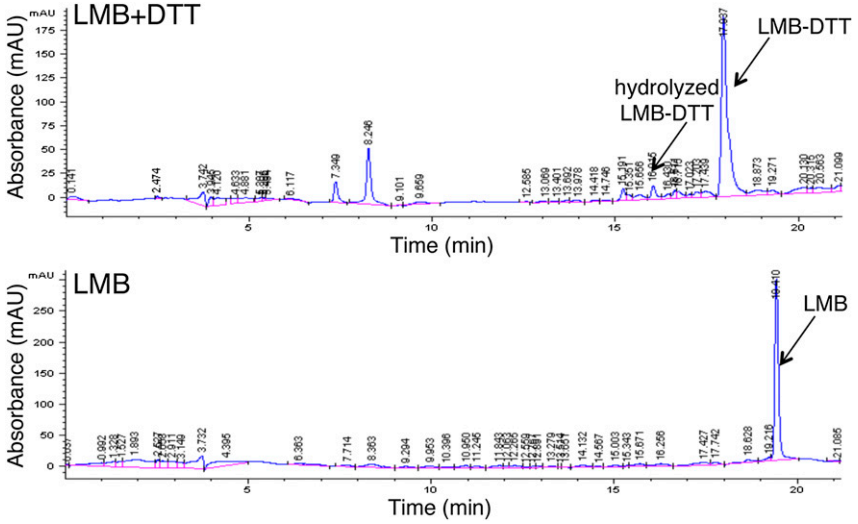


**Fig. S10.** Intrinsic hydrolysis of LMB vs. thiol-conjugated LMB. HPLC traces (detection at 254 nm; pink trace is baseline) is used to quantitate the extent of LMB hydrolysis under various conditions. (*Upper*) LMB and DTT were incubated for 26 h in buffer containing 10 mM Tris, pH 7.5, 100 mM sodium chloride, and 5 mM magnesium acetate before HPLC separation. The HPLC trace shows that the majority of the material is composed of the LMB-DTT adduct with <10% hydrolyzed LMB-DTT and no detectable LMB. DTT did not react with the disubstituted tail unsaturated acid of LMB. (*Lower*) LMB alone (without DTT) in buffer for 26 h shows only the presence of LMB.

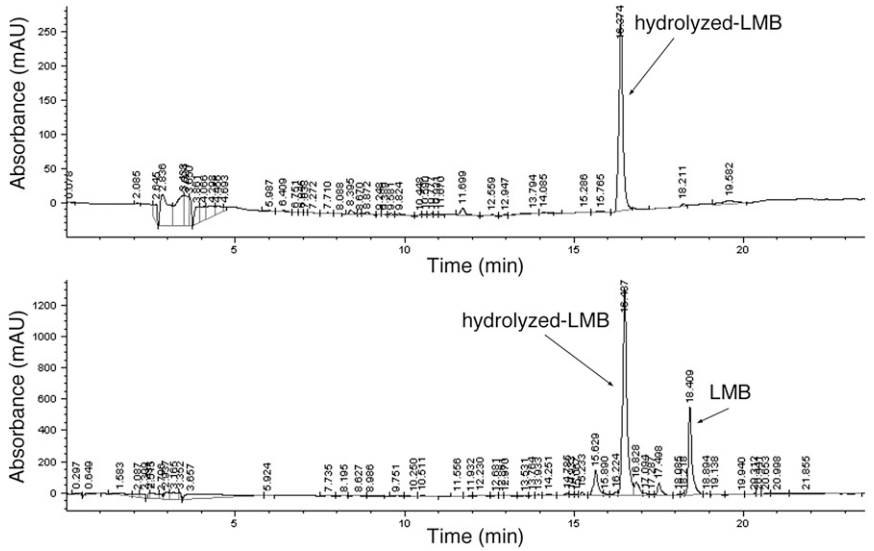


**Fig. S11.** Stability of chemically hydrolyzed LMB. HPLC traces (detection at 254 nm) are used to monitor the stability of chemically hydrolyzed LMB in buffer at pH 7.5. (*Upper*) Chemically hydrolyzed LMB analyzed immediately after HPLC purification. (*Lower*) The same sample, after storage at −20 °C for 20 d, gives a 3:1 ratio of hydrolyzed LMB (1) to LMB.

1. Neville M, Rosbash M (1999) The NES-Crm1p export pathway is not a major mRNA export route in Saccharomyces cerevisiae. *EMBO J* 18(13):3746–3756.

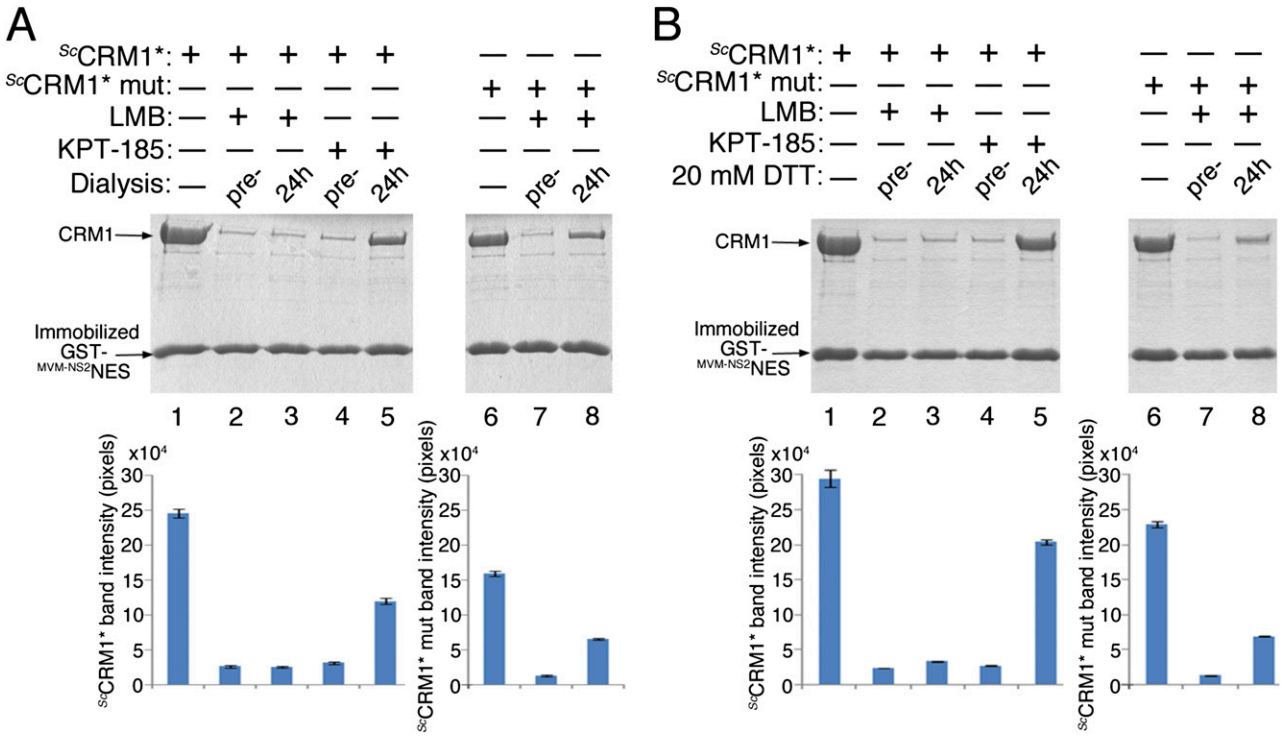


**Fig. S12.** Stability of inhibitor conjugation to CRM1. $^{Sc}$CRM1* or mutant $^{Sc}$CRM1*(K541Q,K542Q,R543S,K545Q,K548Q,K579Q) was incubated with LMB or KPT-185 to achieve full CRM1 inhibition before dialysis of the samples (*A*) or treatment with 20 mM DTT (*B*) to remove excess unbound inhibitor. The extent of CRM1 inhibition was determined using pull-down inhibition assays with immobilized GST-NES, and the proteins were separated by SDS/PAGE and visualized with Coomassie staining. The gels shown here are identical to those gels in Fig. 6 *C* and *D*. Scanned images of the dried gels were processed with the ImageJ software. The intensity of each CRM1 is corrected for the slightly different intensities of the GST-NES bands (lane 1 is the reference for lanes 1–5; lane 6 is the reference for lanes 6–8). The gel was scanned three times, and average intensities and errors of the CRM1 bands were plotted on histograms. In the dialysis experiment (*A*), CRM1 band intensities in lanes 3 and 5 appear to be ∼10% and ∼48%, respectively, compared with the intensity in lane 1. The CRM1 band intensity in lane 8 is ∼41% compared with the reference in lane 6. In the DTT experiment (*B*), the CRM1 band intensities in lanes 3 and 5 appear to be ∼11% and ∼70%, respectively, compared with the intensity in lane 1. The CRM1 band intensity in lane 8 is ∼30% compared with the reference in lane 6.

**Table S1. Crystallographic statistics of LMB, RJA, and AGA**

| | LMB-$^{sc}$CRM1*-$^{hs}$Ran-$^{sc}$RanBP1 | RJA-$^{sc}$CRM1*-$^{hs}$Ran-$^{sc}$RanBP1 | AGA-$^{sc}$CRM1*-$^{hs}$Ran-$^{sc}$RanBP1 |
|---|---|---|---|
| Cell axial lengths (Å) | $a = b = 105.68$, $c = 305.51$ | $a = b = 106.18$, $c = 306.02$ | $a = b = 106.24$, $c = 306.39$ |
| Space group | $P4_32_12$ | $P4_32_12$ | $P4_32_12$ |
| Data collection | | | |
| Resolution range (Å) | 50.00–1.78 (1.81–1.78)* | 50.00–2.00 (2.03–2.00) | 50.00–2.00 (2.03–2.00) |
| Number of observed reflections | 831,144 (15,960) | 746,547 (28,705) | 609,824 (18,284) |
| Number of unique reflections | 162,677 (6,650) | 117,980 (5,741) | 113,527 (5,224) |
| Completeness (%) | 97.8 (81.4) | 99.1 (98.3) | 95.2 (89.2) |
| Redundancy | 5.2 (2.4) | 6.3 (5.0) | 5.5 (3.5) |
| $R_{sym}$[a] (%) | 5.0 (48.2) | 6.8 (51.5) | 6.6 (49.6) |
| Mean $I/I_\sigma$ | 29.0 (1.9) | 22.0 (1.7) | 19.7 (2.0) |
| Solvent content (%) | 56.8 | 57.2 | 57.3 |
| Refinement | | | |
| Resolution range (Å) | 50.00–1.78 (1.83–1.78) | 50.00–2.00 (2.05–2.00) | 50.00–2.00 (2.05–2.00) |
| Number of working reflections | 155,808 (9,319) | 106,441 (7,546) | 101,676 (7,348) |
| Number of test reflections | 3,272 (206) | 5,905 (421) | 5,667 (378) |
| $R_{work}$[b] | 0.136 (0.203) | 0.165 (0.244) | 0.181 (0.357) |
| $R_{free}$[c] | 0.172 (0.263) | 0.212 (0.275) | 0.222 (0.382) |
| rmsd bond lengths (Å) | 0.007 | 0.009 | 0.007 |
| rmsd bond angles (°) | 1.080 | 1.200 | 1.225 |
| Average B factors (Å$^2$) | | | |
| Protein atoms | 31.3 (11,105)[†] | 29.2 (11,212) | 32.3 (11,198) |
| Inhibitor atoms | 39.9 (40) | 38.1 (34) | 57.5 (38) |
| Waters atoms | 47.6 (1,655) | 46.1 (1,359) | 47.3 (975) |
| Ramachandran plot | | | |
| Most favored (%) | 94.5 | 94.1 | 93.8 |
| Allowed (%) | 5.3 | 5.6 | 5.9 |
| General allowed (%) | 0.1 | 0.2 | 0.2 |
| Disallowed (%) | 0.1 | 0.1 | 0.1 |

$R^a_{sym} = \sum |I_i - <I>| / \sum |I_i|$, $I_i$ is the intensity of the $i$th measurement, and $<I>$ is the mean intensity for that reflection $R^b_{work} = \sum |Fo - Fc| / |Fo|$. Fc and Fo are the calculated and observed structure factor amplitudes, respectively. $R_{free}$[c] was calculated as for $R_{work}$ but for 5.0% of the total reflections chosen at random and omitted from refinement for all datasets.

*Values for highest resolution shell.

[†]Number of atoms.

**Table S2. Crystallographic statistics of unliganded $^{sc}$CRM1* and CRM1 mutants**

| | $^{sc}$CRM1*-$^{hs}$Ran-$^{sc}$RanBP1 | $^{sc}$CRM1(T539S)-$^{hs}$Ran-$^{sc}$RanBP1 | LMB-$^{sc}$CRM1($^{537}$DLTVK$^{541}$/GLCEQ)-$^{hs}$ Ran-$^{sc}$RanBP1 |
|---|---|---|---|
| Cell axial lengths (Å) | $a = b = 106.32$, $c = 306.69$ | $a = b = 106.12$, $c = 305.43$ | *$a = b = 105.97$, $c = 304.93$* |
| Space group | $P4_32_12$ | $P4_32_12$ | $P4_32_12$ |
| Data collection | | | |
| Resolution range (Å) | 50.00–1.80 (1.83–1.80) | 50.00–2.80 (2.85–2.80) | 50.00–2.05 (2.09–2.05) |
| Number of observed reflections | 889,236 (27,458) | 313,511 (8,860) | 1,111,886 (39,398) |
| Number of unique reflections | 161,279 (7,845) | 42,836 (1,969) | 109,601 (5,397) |
| Completeness (%) | 99.0 (97.7) | 96.7 (92.3) | 99.8 (99.7) |
| Redundancy | 5.6 (3.5) | 7.4 (4.5) | 10.2 (7.3) |
| $R_{sym}$[a] (%) | 6.5 (44.1) | 14.6 (55.4) | 10.1 (62.4) |
| Mean $I/I_\sigma$ | 21.2 (2.0) | 11.5 (1.6) | 18.7 (1.9) |
| Solvent content (%) | 57.5 | 57.8 | 56.6 |
| Refinement | | | |
| Resolution range (Å) | 50.00–1.80 (1.85–1.80) | 50.00–2.80 (2.87–2.80) | 50.00–2.05 (2.10–2.05) |
| Number of working reflections | 145,664 (11,024) | 38,486 (2,559) | 99,871 (7,065) |
| Number of test reflections | 8,105 (596) | 2,151 (139) | 5,473 (338) |
| $R_{work}$[b] | 0.166 (0.287) | 0.234 (0.443) | 0.187 (0.384) |
| $R_{free}$[c] | 0.206 (0.314) | 0.276 (0.443) | 0.216 (0.391) |
| rmsd bond lengths (Å) | 0.014 | 0.007 | 0.008 |
| rmsd bond angles (°) | 1.318 | 0.993 | 1.182 |
| Average B factors (Å$^2$) | | | |
| Protein atoms | 25.3 (11,291) | 62.5 (10,993) | 30.5 (11,121) |
| Inhibitor atoms | Not applicable | Not applicable | 34.9 (40) |
| Waters atoms | 36.1 (1,381) | 60.6 (68) | 49.0 (860) |
| Ramachandran plot | | | |
| Most favored (%) | 93.9 | 92.6 | 93.9 |
| Allowed (%) | 5.8 | 7.1 | 5.8 |
| General allowed (%) | 0.2 | 0.1 | 0.2 |
| Disallowed (%) | 0.1 | 0.2 | 0.2 |

$R^a_{sym} = \sum |I_i - <I>| / \sum |I_i|$, where $I_i$ is the intensity of the *i*th measurement, and <I> is the mean intensity for that reflection $R^b_{work} = \sum |Fo - Fc| / |Fo|$, where Fc and Fo are the calculated and observed structure factor amplitudes, respectively. $R^c_{free}$ is calculated as for $R_{work}$ but for 5.0% of the total reflections chosen at random and omitted from refinement for all datasets.

**Table S3. Crystallographic statistics of mutant $^{sc}$CRM1*(K548A) and $^{sc}$CRM1*(K579A) complexes**

| | LMB- $^{sc}$CRM1*(K548A)-$^{hs}$Ran-$^{sc}$RanBP1 | RJA- $^{sc}$CRM1*(K579A)-$^{hs}$Ran-$^{sc}$RanBP1 |
|---|---|---|
| Cell axial lengths (Å) | $a = b = 106.57$, $c = 306.97$ | $a = b = 106.19$, $c = 306.07$ |
| Space group | $P4_32_12$ | $P4_32_12$ |
| Data collection | | |
| Resolution range (Å) | 50.00–1.90 (1.93–1.90)* | 50.00–2.28 (2.32–2.28) |
| Number of observed reflections | 1,021,314 (19,971) | 825,797 (26,612) |
| Number of unique reflections | 135,716 (5,874) | 80,721 (3,972) |
| Completeness (%) | 97.0 (85.0) | 99.8 (99.7) |
| Redundancy | 7.6 (3.4) | 10.2 (6.7) |
| $R_{sym}$[a] (%) | 6.5 (49.1) | 7.0 (49.9) |
| Mean $I/I_\sigma$ | 25.1 (2) | 27.1 (2.5) |
| Solvent content (%) | 57.7 | 57.3 |
| Refinement | | |
| Resolution range (Å) | 50.00–1.90 (1.95–1.90) | 50–2.28 (2.34–2.28) |
| Number of working reflections | 122,370 (7,956) | 72,784 (5,114) |
| Number of test reflections | 6,802 (406) | 4,051 (280) |
| $R_{work}$[b] | 0.164 (0.317) | 0.166 (0.267) |
| $R_{free}$[c] | 0.209 (0.407) | 0.213 (0.316) |
| rmsd bond lengths (Å) | 0.007 | 0.009 |
| rmsd bond angles (°) | 1.049 | 1.230 |
| Average B factors (Å$^2$) | | |
| Protein atoms | 32.9 (11,036)[†] | 39.2 (11,233) |
| Inhibitor atoms | 41.8 (40) | 49.1 (34) |
| Waters atoms | 49.8 (1,438) | 54.5 (1,089) |
| Ramachandran plot | | |
| Most favored (%) | 94.5 | 93.9 |
| Allowed (%) | 5.3 | 5.7 |
| General allowed (%) | 0.0 | 0.3 |
| Disallowed (%) | 0.2 | 0.1 |

$R^a_{sym} = \sum |I_i - <I>| / \sum |I_i|$, where $I_i$ is the intensity of the *i*th measurement, and <I> is the mean intensity for that reflection $R^b_{work} = \sum |Fo - Fc| / |Fo|$, where Fc and Fo are the calculated and observed structure factor amplitudes, respectively. $R^c_{free}$ is calculated as for $R_{work}$ but for 5.0% of the total reflections chosen at random and omitted from refinement for all datasets.

*Values for highest resolution shell.

[†]Number of atoms.

**Table S4. Crystallographic statistics of CRM1 with basic residues mutated**

| | LMB-$^{sc}$CRM1*(K548E, K579Q)-$^{hs}$Ran-$^{sc}$RanBP1 | LMB- $^{sc}$CRM1*(R543S, K548E, K579Q)-$^{hs}$Ran-$^{sc}$RanBP1 | LMB-$^{sc}$CRM1*(K541Q, K542Q, R543S, K545Q, K548Q, K579Q)-$^{hs}$Ran-$^{sc}$RanBP1 |
|---|---|---|---|
| Cell axial lengths (Å) | *a = b = 106.17, c = 305.67* | *a = b* = 105.82, *c* = 305.23 | *a = b* = 105.54, *c* = 305.04 |
| Space group | $P4_32_12$ | $P4_32_12$ | $P4_32_12$ |
| Data collection | | | |
| Resolution range (Å) | 50.00–2.30 (2.34–2.30) | 50.00–1.90 (1.93–1.90) | 50.00–2.20 (2.24–2.20) |
| Number of observed reflections | 655,495 (16,924) | 1,327,905 (31,434) | 449,926 (18,678) |
| Number of unique reflections | 77,568 (3,601) | 136,841 (6,688) | 87,149 (4,245) |
| Completeness (%) | 97.9 (93.1) | 99.8 (99.0) | 98.0 (97.3) |
| Redundancy | 8.5 (4.7) | 9.7 (4.7) | 5.2 (4.6) |
| $R_{sym}$[a] (%) | 11.4 (61.8) | 10.7 (61.4) | 11.2 (51.6) |
| Mean $I/I_\sigma$ | 15.9 (1.5) | 18.0 (1.7) | 12.3 (1.7) |
| Solvent content (%) | 57.2 | 56.8 | 56.6 |
| Refinement | | | |
| Resolution range (Å) | 50.00–2.30 (2.36–2.30) | 50.00–1.90 (1.95–1.90) | 50.00–2.20 (2.26–2.20) |
| Number of working reflections | 69,563 (4,745) | 123,361 (8,708) | 78,220 (5,544) |
| Number of test reflections | 3,888 (247) | 6,882 (494) | 4,364 (265) |
| $R_{work}$[b] | 0.186 (0.346) | 0.168 (0.377) | 0.186 (0.327) |
| $R_{free}$[c] | 0.228 (0.352) | 0.208 (0.409) | 0.225 (0.357) |
| rmsd bond lengths (Å) | 0.014 | 0.005 | 0.014 |
| rmsd bond angles (°) | 1.361 | 0.0965 | 1.508 |
| Average B factors (Å$^2$) | | | |
| Protein atoms | 40.0 (11,200)* | 28.7 (11,012) | 35.9 (11,036) |
| Inhibitor atoms | 50.9 (40) | 33.3 (39) | 49.2 (39) |
| Waters atoms | 54.3 (677) | 44.9 (1,177) | 36.0 (790) |
| Ramachandran plot | | | |
| Most favored (%) | 94.6 | 94.6 | 94.1 |
| Allowed (%) | 5.2 | 5.3 | 5.6 |
| General allowed (%) | 0.1 | 0.0 | 0.2 |
| Disallowed (%) | 0.2 | 0.2 | 0.2 |

$R^a_{sym} = \sum |I_i - <I>| / \sum |I_i|$. $I_i$ is the intensity of the *i*th measurement, and <I> is the mean intensity for that reflection $R^b_{work} = \sum |Fo - Fc| / |Fo|$. Fc and Fo are the calculated and observed structure factor amplitudes, respectively. $R^c_{free}$ is calculated as for $R_{work}$ but for 5.0% of the total reflections chosen at random and omitted from refinement for all datasets.
*Number of atom.

**Table S5. Hydrolysis of LMB vs. thiol-conjugated LMB**

| Time (h) | Thiol | LMB* | DTT-LMB* | Hydrolyzed DTT-LMB* |
|---|---|---|---|---|
| 26 | — | 1 | 0 | 0 |
| 26 | DTT | 0 | 1 | 0.10 |

*Ratios are based off integration of LC chromatogram at 254 nm.